Xu, Z., Melville, B. W., Wotherspoon, L., & Nandasena, N. A. K. (2020). Stability of composite breakwaters under tsunami attack. Journal of Waterway, Port, Coastal and Ocean Engineering, 146(4). https://doi.org/10.1061/(ASCE)WW.1943-5460.0000571

Stability of Composite Breakwaters under Tsunami Attack

Zhonghou Xu[1], Bruce W. Melville[2], Liam Wotherspoon[3], N. A. K. Nandasena[4]

1 Doctoral Student, Department of Civil and Environmental Engineering, The University of Auckland, Auckland, 1142, New Zealand. Email: zxu159@aucklanduni.ac.nz

2 Professor, Department of Civil and Environmental Engineering, The University of Auckland, Auckland, 1142, New Zealand. Email: b.melville@auckland.ac.nz

3 Associate Professor, Department of Civil and Environmental Engineering, The University of Auckland, Auckland, 1142, New Zealand. Email: l.wotherspoon@auckland.ac.nz

4 Assistant Professor, Department of Civil and Environmental Engineering, United Arab Emirates University, Al Ain, 15551, United Arab Emirates. Email: kithsiri1978@yahoo.com

Abstract

Breakwaters are effective structures for mitigating tsunami-induced damage. However, pieces of the breakwater can be displaced by the turbulent tsunami flow, which undermines the stability of the breakwater and reduces its mitigation effectiveness. Assessing the damage to breakwaters in tsunami-prone coasts is therefore valuable for the port authority, cargo owners and coastal residents. Physical experiments were conducted to assess potential damage to a typical composite breakwater in New Zealand due to tsunamis. Higher breakwaters can resist a stronger bore impact and experienced delayed initiation of the same damage. A new parameter is proposed to assess the damage in the armour layer which takes into account the size and density of armour units, height of the breakwater and the tsunami bore depth.

Keywords: breakwater, tsunami, damage, stability, dam-break flow

1. Introduction

Tsunamis are destructive coastal hazards that pose threats to coastal regions. Coastal structures such as rubble mound breakwaters and seawalls can provide shelter from devastating tsunamis (Chen et al., 2018; Nandasena et al., 2012; Takagi and Bricker, 2014). These coastal structures need to be stable during a tsunami to play their role in reducing its impact. Recent tsunamis (e.g. the 2004 Indian Ocean Tsunami and the 2011 Tohoku Earthquake and Tsunami) have caused significant damage to breakwaters and seawalls, transporting armour units and blocks inland (Lekkas et al., 2011; Nandasena et al., 2011a; PARI, 2011; Paris et al., 2010). Many factors could lead to the collapse of coastal structures, including: the water level difference between the seaside and leeside of the structure (Arikawa et al., 2012), leeside scour (Kato et al., 2012), and tilting and sliding of caissons (Takagi and

Esteban, 2013). Following field surveys of damaged coastal structures in Miyagi and Fukushima prefecture after the 2011 Great Japan Tsunami, Jayaratne et al. (2016) summarised failure modes for dikes and seawalls, i.e., leeward and seaward toe scour failure, leeward and seaward slope armour failure, crown armour failure, parapet wall failure and overturning failure. Esteban et al. (2014) analysed the stability of breakwaters struck by the 2004 Indian Ocean Tsunami and the 2011 Great Japan Tsunami, and used a damage parameter similar to that used by Van der Meer (1987) to define the damage level of armour units of breakwaters under tsunami attack. The stability of harbour side breakwater units due to tsunami overflow has been studied using physical and numerical modelling (Maruyama et al., 2014; Mitsui et al., 2014, 2016). Due to the limited applicability of the downes formulae (Isbash, 1936), an estimation method based on overflow depth was established to determine the required mass of armour units (Mitsui et al., 2016). Experimental investigations of tsunami waves impacting rubble mound breakwaters have been carried out with solitary waves and wave overflow approaches (Aniel-Quiroga et al., 2018; Guler et al., 2015). Aniel-Quiroga et al. (2018) took into consideration the damage parameter, the freeboard, the stability number and the number of waves. They found that the tsunami-induced damage of the armour units evolves faster than that by wind waves. Gómez-Martín and Medina (2013) classified the evolution of the armour damage under waves into the four stages listed below, based on the previous armour damage criteria proposed by Losada et al. (1986) and Vidal et al.(1991): (1) Initiation of damage, when the upper armour layer has lost some units; (2) Initiation of Iribarren's damage, when the bottom armour layer is exposed and units in the layer can be extracted due to the damage in the upper armour layer; (3) Initiation of destruction, when the units from the bottom armour layer are removed and the filter layer is visible; and (4) Destruction, when several units have been removed from the filter layer.

This study was undertaken to better understand tsunami flow-breakwater interaction and the potential failure modes for composite breakwaters under a range of tsunami depths, the failure modes including armour movement and movement of other breakwater elements. A breakwater in New Zealand (Napier Port breakwater) was chosen as a typical tsunami-prone composite breakwater. Napier Port is the fourth largest container terminal in New Zealand (Napier Port Ltd, 2018). Sheltered by a robust breakwater, the port lies in Hawke's Bay, which is 120 km to the west of the Hikurangi Trough in the South Pacific Ocean (Fig. 1a). The Hikurangi subduction zone is a potential source of tsunamigenic earthquakes (Fraser et al., 2014; GNS Science, 2013). Near Hawke's Bay, a slow-slip earthquake off the coast of Gisborne on 26 March, 1947 (M_w: 7.0-7.1) generated one of the largest tsunamis in New Zealand's recorded history, with a maximum run-up of 10 m in Gisborne (Downes et al., 2000). The return period of the 1947 tsunami was estimated to be 500 years (Fraser, 1998) and the wave period of was 3~10 min according to local eyewitnesses (Eiby, 1982). The 1960 Chile Tsunami caused a maximum run-up of 4.5 m on the East Coast of Napier (King, 2015). The maximum tsunami flow depth could exceed 8 m onshore in Napier under extreme conditions (rupture of the whole Hikurangi subduction margin), according to the numerical estimation of Fraser et al. (2014).

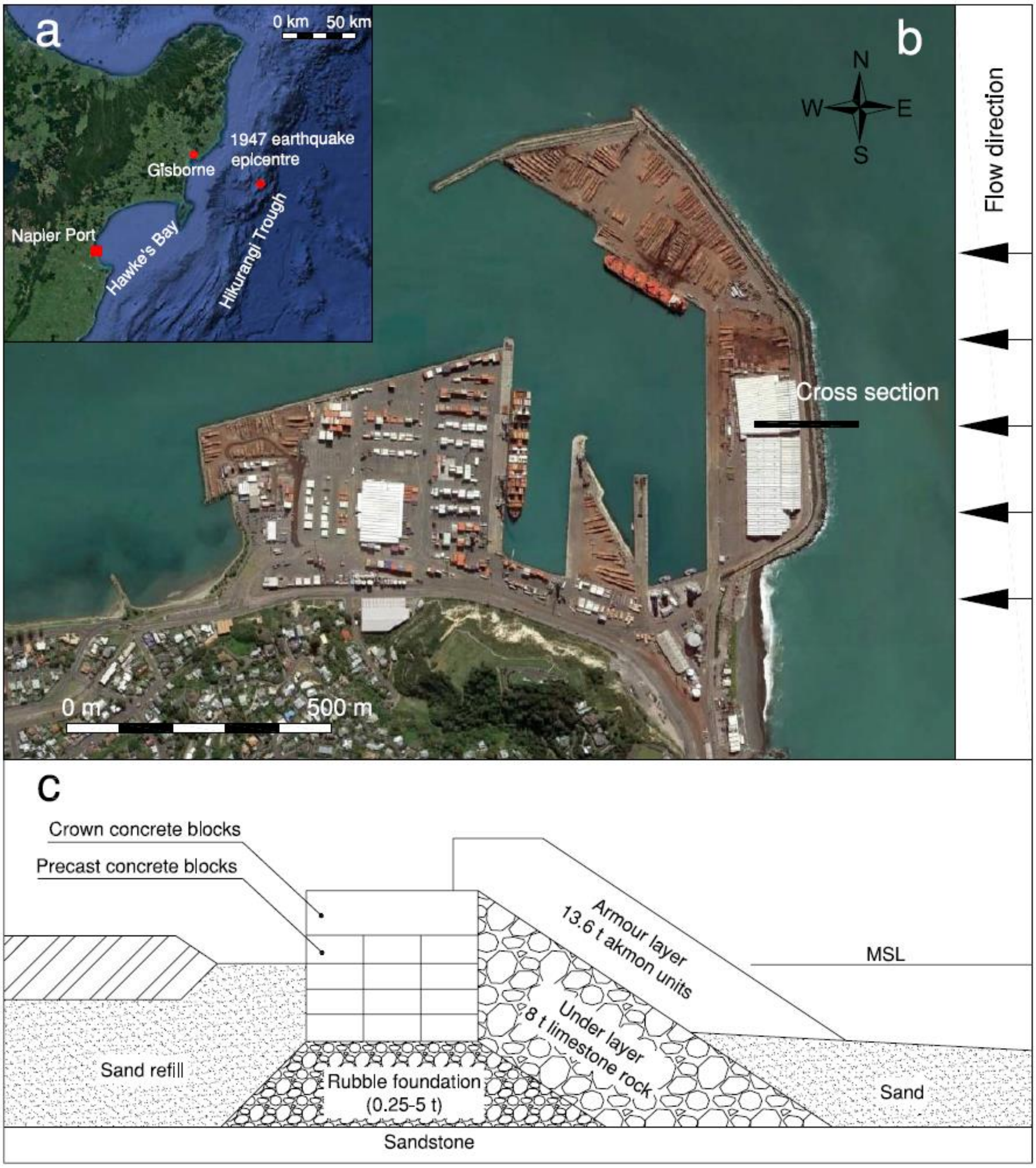

Fig. 1 (a) Location of Napier Port in Hawke's Bay, (b) location of the studied cross section in Napier Port breakwater, (c) simplified schematic of the studied cross section and its composition. Sources: Google Earth, GeoNet, Opus (2018).

2. Methodology

2.1 Facility

Physical experiments were carried out in the Fluid Mechanics Laboratory at the University of Auckland, New Zealand. The tsunami flume consists of a 19.2 m long, 1.2 m wide and 1.2 m deep channel and a reservoir 6.4 m long, 5.5 m wide and 1.2 m deep (Fig. 2). The reservoir covers an area of 30 m^2 and has a maximum storage capacity of 36 m^3 water. An automatic gate is installed at one end of the channel to generate a tsunami-like bore. The drain gate and outlet are used to empty the flume. The automatic gate is opened for 10 s to generate stable bores, which were used to simulate tsunami bores due to the similarity of dam-break flows to the motion of tsunami bores (Chanson, 2006).

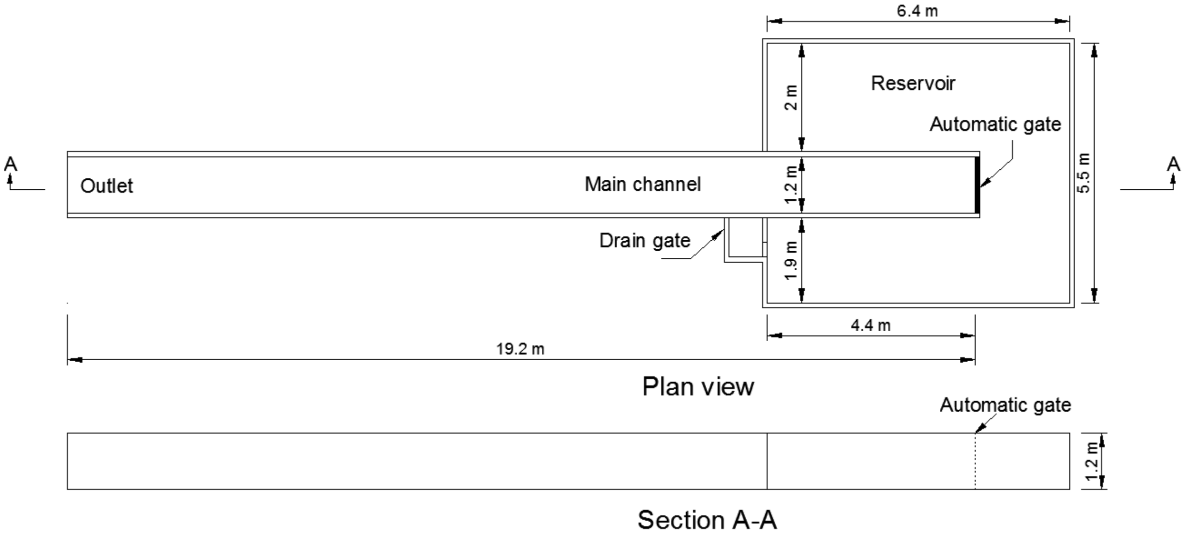

Fig. 2 Experimental set-up: plan view of the tsunami flume and side view of the flume

2.2. Description of scaled models

The typical cross-section of the Napier Port breakwater was developed based on available drawings and schematics (Opus, 2018). Fig. 1b shows the location of the cross section through the breakwater, which faces due east (offshore direction). The selected breakwater cross section is a composite structure, including a seaward armour layer (13.6 t Akmon units in two layers), an underlayer comprised of 8 t (W_{50}) limestone rocks, crown concrete blocks and precast concrete blocks in four layers. The leeside of the breakwater is reclaimed and forms a storage yard (Fig. 1c). The tidal range at Napier Port is approximately 1.5 m and was not considered in this study. The water level was assumed to be mean sea level (MSL in Fig. 1c) before the arrival of a tsunami wave. Typically the highest tidal level was considered for analysis as it represents the worst case, but in this study we simulated complete sea withdrawal before the first wave (bore) came. Therefore, rather than considering tides and waves, we considered the flow depth from the bed (more details are given in section 2.3).

Due to the dominant role of inertial and gravitational forces in tsunami wave motion and their effect on structures, the scaling is based on Froude number similarity. Typical breakwater sections with four different heights were reproduced at a 1:40 length scale. The stability of armour units can be simulated correctly when the weight scale is computed using Eq. (1)

$$\lambda_W = (\lambda_L^3)\frac{(\gamma_r)_m}{(\gamma_r)_p}\left[\frac{(\gamma_r)_p/(\gamma_W)_p - 1}{(\gamma_r)_m/(\gamma_W)_m - 1}\right]^3 \tag{1}$$

where $(\gamma_r)_m$ and $(\gamma_r)_p$ are the densities of stones in model and prototype, $(\gamma_W)_m$ is the unit weight of water used in the model, which is 1000 kg/m^3 and $(\gamma_W)_p$ is the unit weight of sea water, which is assumed to be 1025 kg/m^3. The densities of limestone rocks, Akmon units and concrete blocks are 2400 kg/m^3 in the model and prototype. Hence, the scales are: length scale=λ_L=40, time scale=λ_T=6.32, and weight scale =λ_W=56303 (Akmon units, limestone rocks and concrete blocks). The details of units used in experiments are given in Table 1. These four types of units were moveable in this experiment while the structure behind the breakwater was fixed to simulate the storage yard, thus the potential leeside erosion during tsunami overflow was not simulated.

Table 1 Summary of units and blocks used in experiments. Note *a*, *b*, and *c* are the lengths of longitudinal, lateral, and height axes of the concrete blocks, respectively.

Units	Density (kg/m^3)	Model weight (g)	Dimension (mm), ($a \times b \times c$)	Number
Akmon units	2400	242	-	298
Limestone rocks	2400	142 (W_{50})	-	621
Crown concrete blocks	2400	4394	$264 \times 95 \times 73$	12
Precast concrete blocks	2400	436	$88 \times 48 \times 43$	288

Fig. 3 shows the scaled model cross sections of the breakwater for four different breakwater heights, with 1 to 4 layers of precast concrete blocks behind the armour units, for which the breakwater heights above the base of the flume (h_b) were 116 mm, 159 mm, 202 mm and 245 mm. The precast concrete blocks were placed in 3 rows (24 blocks each row) along the flume. On top of the precast concrete blocks, the 12 crown concrete blocks were aligned longitudinally in one row across the width of the flume (with their longitudinal axes aligned along the flume). The setup was the same for different layers of the precast concrete blocks. The centreline of the crown concrete blocks was 13.2 m downstream of the pneumatic gate from which the tsunami-like bore is released.

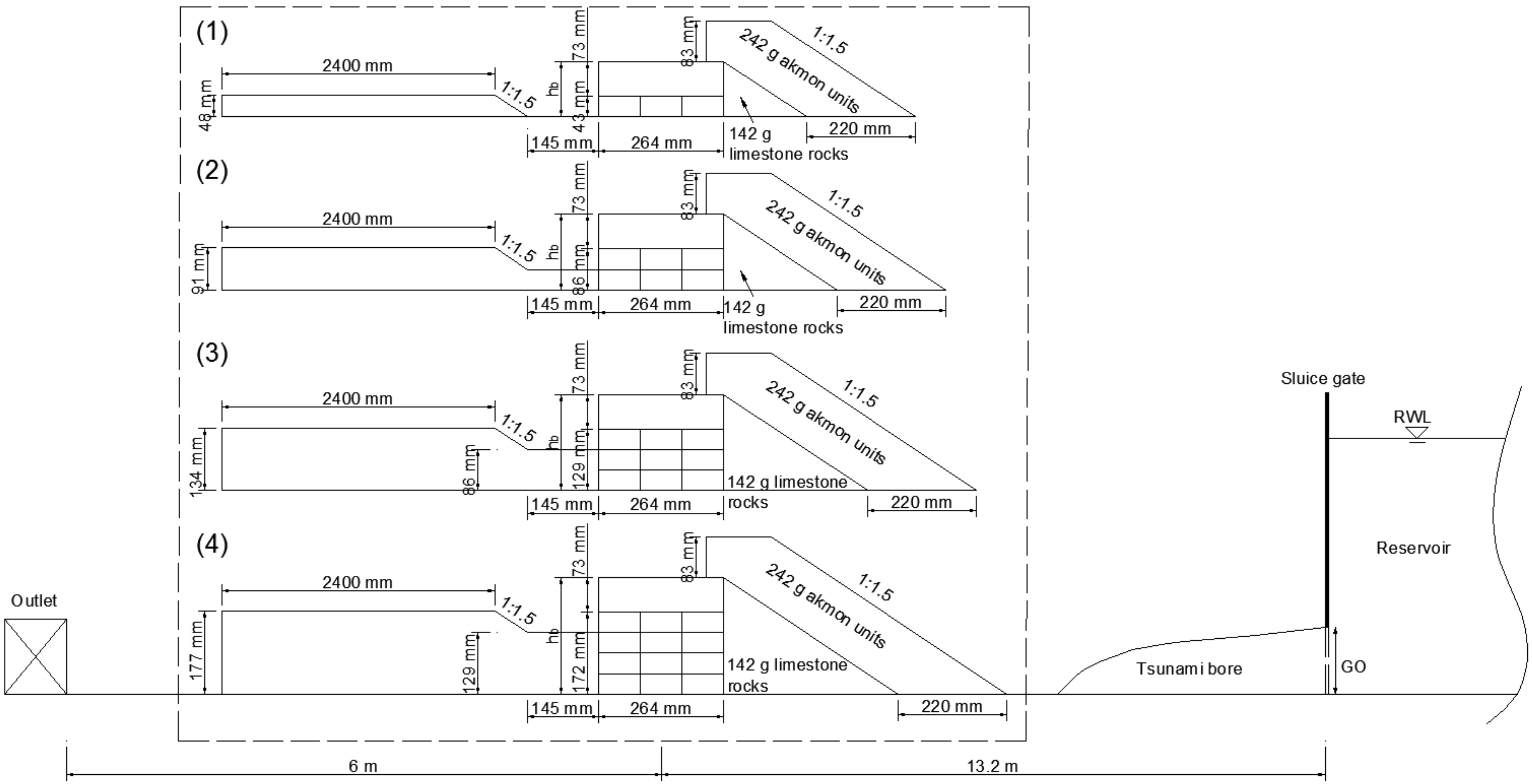

Fig. 3 Model set-up with different breakwater heights: (1) 116 mm; (2) 159 mm; (3) 202 mm; (4) 245 mm. h_b is the breakwater height. *RWL* is the reservoir water level and *GO* is the gate opening height. (Figure not to scale)

2.3. Experimental conditions and procedure

Tsunami propagation was carried out on a dry flume bed, which simulates conditions with an exposed seaward bed caused by water recession before the first tsunami wave strikes (Fritz et al., 2011, 2007; Goto et al., 2007; Klettner et al., 2012; Tadepalli and Synolakis, 1996). As shown in Fig. 1, the breakwater is very close to the beach, with one end connected to the beach. The potential water recession when a tsunami occurs could expose the seabed at the seaside of the breakwater, especially the part close to the beach. The set-up with different breakwater heights enables analysis of the tsunami impact along the breakwater (cross-sections being similar) as the seabed level changes. In addition, it allows analysis of the influence of breakwater heights for a range of tsunami bores. Seven dam-break generated tsunami bores were used (detailed description in section 3.1). Before the model was constructed, maximum bore depths and bore tip propagation speeds along the flume were measured in the tsunami flume using four capacitance wave gauges spaced 1.5 m apart along centreline of the flume following the method of Chen et al. (2016) and Shafiei et al. (2016). The bore tip propagation speed was calculated by dividing the distance between two gauges and the time difference between when the bore hit the wave gauges (time of flight approach). The last wave gauge was mounted 12.7 m downstream of the gate on the centreline of the flume, with a side-looking Nortec Vectrino acoustic Doppler velocimeter (ADV) 40 mm above the flume bed. Bore depths were measured at 1000 Hz and velocities were measured at 200 Hz simultaneously. Five repetitions of each size of bore were conducted to get consistent and reliable results. The gate was opened almost instantaneously to the gate opening height (*GO*) and remained open for 10 s before closing automatically. For each of the bore cases, at least five trials were run and the breakwater was rebuilt after each trial. Through this rebuilding process, the effect of variation in placement of breakwater components could be assessed, as the rebuilding process does not result in identical layouts. In the experiments, the seaward Akmon units, limestone rocks and concrete blocks were all moveable. Damage of the armour layer and the body of the breakwater and displacement of the Akmon units and concrete blocks was measured. Measurements of the damaged armour layer and underlayer were made in the central area of the flume (0.8 m in length). The Akmon units and limestone rocks outside the measured section were dyed black. The Akmon units in the measured section were dyed in three colours, yellow for the upper part, red for the middle and green for the lower part. The precast concrete blocks in different layers and rows were marked differently so that the path taken by an extracted block could be tracked. A detailed summary of the model composition is given in Table 2. Three cameras, one top view (GoPro 6, 60 fps), one side view (Webcam 920, 30 fps) and one lateral view (Webcam 920, 30 fps) were installed to capture the flow interaction with the structure.

Table 2 Composition of each model in terms of the number of different breakwater components

Breakwater height h_b	Number of Akmon units (two layers)					Number of limestone rocks			Number of precast concrete blocks	Number of precast blocks layers
mm	Yellow (upper centre)	Red (middle centre)	Green (lower centre)	Black (both sides)	Total	White (centre)	Black (both sides)	Total		
116	38	38	38	54	168	101	50	151	72	1
159	48	48	48	78	222	178	88	264	144	2
202	55	57	57	83	252	250	130	380	216	3
245	66	66	66	100	298	405	216	621	288	4

2.4. Damage assessment methodology

Both visual and quantitative methods were used to analyse the damage of the breakwater. The quantitative damage assessment of the armour layer was analysed with the following parameters.

The stability number proposed by Hudson (1959) was calculated, using Eq. (2), i.e.,

$$N_s = \frac{h_0}{\Delta D_{n50}} \tag{2}$$

where Δ is the relative mass density given by $\Delta=\rho_s/\rho_w-1$, in which ρ_s and ρ_w are densities of the breakwater units and water respectively and h_0 is the bore depth, which was used instead of the significant wave height as used by Hudson (1959). D_{n50} is the cube-equivalent side length of the Akmon units (0.0465 m). N_s can be considered to be the ratio of the destabilising strength of the bore to the mass of the armour units.

In this study, the breakwater height was normalised in two different ways, as follows,

$$F_n = \frac{h_b}{h_0} \tag{3}$$

$$F_b = \frac{(h_b \Delta D_{n50})^{0.5}}{h_0} \tag{4}$$

where F_n is termed relative breakwater height and F_b is a ratio of the stabilising strength of the armour units to the bore depth.

The damage parameter, S, was used to quantify the damage of the Akmon units in the armour layer. S is defined in equation (5) following Broderick (1984):

$$S = \frac{A_e}{D_{n50}^2} \tag{5}$$

where A_e is the average eroded area, which can be computed using Eq. (6) (Vidal et al., 2004)

$$A_e = \frac{N_e D_{n50}^3}{(1-n)L} \tag{6}$$

where N_e is the number of extracted stones or units, L is the width of the studied section (0.8 m in this study) and n is the armour layer bulk porosity computed as follows,

$$n = \frac{dA - mV}{dA} \quad (7)$$

where A is the surface area of the armour layer (m^2), m is the number of armour units, V is the volume of a single armour unit (m^3) and d is the thickness of the armour layer (m). In this study, n=0.616. The damage ratio, R_d, was also used to quantify the damage of the armour layer; it is defined as the percentage of displaced armour units to the total number of armour units following Hudson (1959)

$$R_d = \frac{N_{displaced}}{N_{total}} \times 100\% \quad (8)$$

where $N_{displaced}$ is the number of displaced stones or units and N_{total} is the total number of stones or units in the section.

3. Results

3.1. Flow depths and velocities

Table 3 shows the bore properties measured at 12.7 m downstream of the pneumatic gate. With a length scale of 1:40, the cases (a)-(g) simulate tsunami bores with heights from 3.68 m to 8.8 m in the prototype. Fig. 4a and Fig. 4b illustrate the time series of the bore depths and velocities (cases b, c, d, g in Table 2). The bore arrival at the wave gauge was characterised by a rapid increase in free surface elevation. A quasi-steady period followed the bore front for approximately 5 s, before the free surface elevation decreased as the gate closed. The model wave half-period $T/2$ exceeded 25 s for all bore cases, equivalent to a real life tsunami $T/2>158$ s. For the velocity measurement, the ADV could not capture data at the leading edge of the bore because of the aeration of the bore front and that the ADV was exposed to the air. A second order polynomial curve was used to fit the temporal dependence of the bore tip propagation speed and the velocities measured by the ADV, as shown in Fig. 4b (Park et al., 2013). The bore has a larger velocity at its front and a steady decreasing trend. Fig. 4c and Fig. 4d illustrate the time series of Froude number Fr and specific momentum flux hu^2. Froude number is defined as:

$$Fr = \frac{u}{\sqrt{gh}} \quad (9)$$

where u is the depth-averaged velocity, h is the water depth and g is gravitational acceleration. A preliminary experiment shows that velocities measured at 40 mm, 80 mm and 120 mm above the flume bed were almost the same. Herein, velocities measured at 40 mm above the flume bed were used to calculate Fr and specific momentum flux hu^2. The Froude number Fr is larger than 3 at the bore front and decreases rapidly after the bore height reached its peak. Fr ranges from 1.05-1.6 in the quasi-steady period for bore cases (a)-(g). The specific momentum flux reached its maximum value before the bore reached its maximum depth.

Table 3 Properties of generated tsunami bores

Case ID	Reservoir water depth *H* (mm)	Gate opening height *GO* (mm)	Gate opening time (s)	Maximum bore depth h_0 (mm)	Bore tip propagation speed *U* (m/s)	Average *Fr* in the quasi-steady period
a	300	200	10	92	1.91	1.05
b	400	200	10	120	2.41	1.49
c	500	200	10	148	2.75	1.47
d	600	200	10	156	2.92	1.49
e	700	200	10	165	3.28	1.67
f	700	300	10	200	3.31	1.39
g	900	300	10	220	4.01	1.60

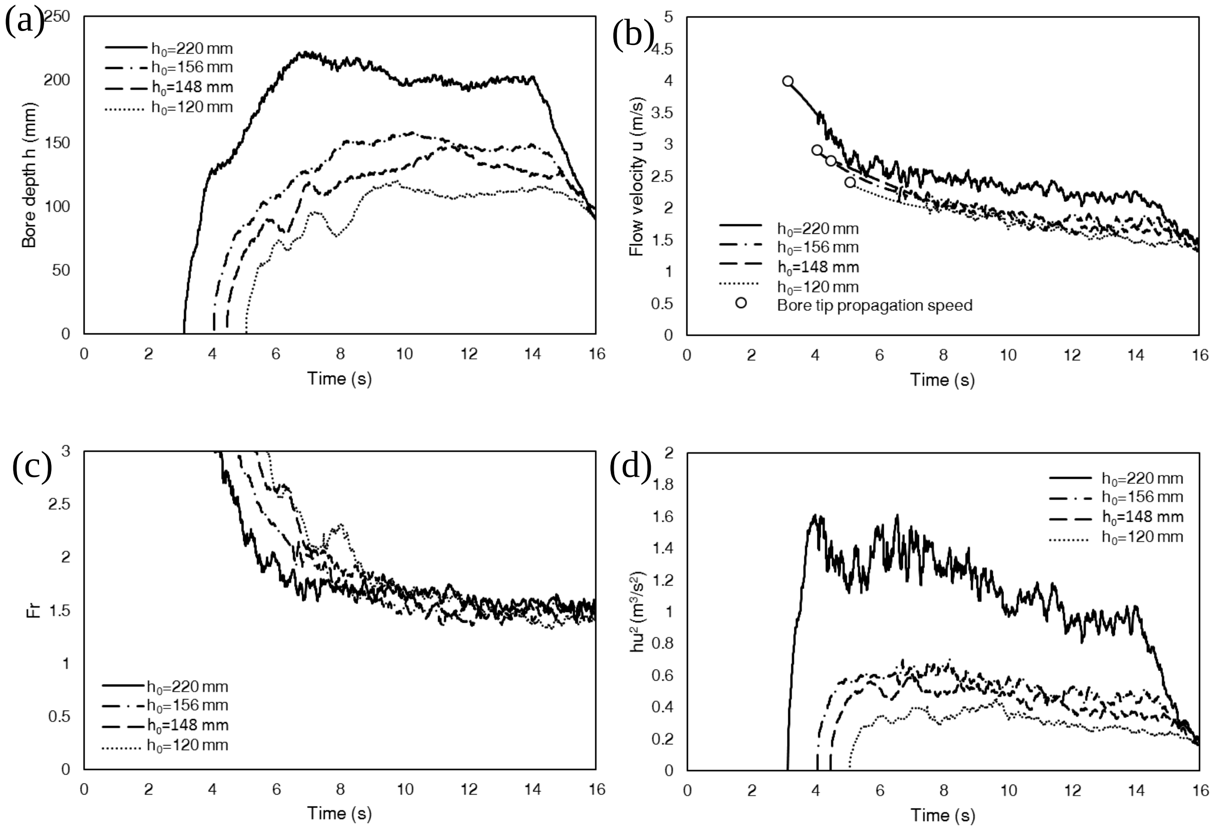

Fig. 4. Time series of (a) bore depth *h*, (b) flow velocity *u*, (c) *Fr* and (d) hu^2 without the breakwater at 12.7 m downstream of the pneumatic gate. Bore cases are b, c, d and g (Table 3). The bore propagation speeds are the circles in (b). A second order polynomial curve was used to fit the bore tip propagation speed and velocities measured by the ADV.

3.2. Flow interaction with the breakwater

The tsunami bores were supercritical flow (Fr>1) before they impacted the breakwater. The water flow splashed up the slope and overtopped the breakwater, which caused air entrainment and energy dissipation. Meanwhile, a significant flow of water was deflected back seawards, forming a feature resembling a hydraulic jump above or upstream of the breakwater, similar to that observed by Ozmen-Cagatay and Kocaman (2011) and Esteban et al. (2017). Fig. 5 shows four stages of the flow impact on the breakwater (h_b=116 mm, h_0=148 mm): (1) initial impact, (2) splash up, (3) overtopping, (4) quasi-steady overflow. The times shown in Fig. 5 are measured from when the bore tip reached the toe of the breakwater. Ohtsu et al. (1996) found that the transition from splash up to a surface roller upstream of the obstacle while increasing the height of an obstacle (termed case A incipient jump) was dependent on the relative obstacle height (termed F_n in this paper) and the supercritical Froude number. Thus, the time spans of the four stages are different for different case combinations. For a stronger bore and the same breakwater height, the case A incipient jump occurred later, as the “jet flow” dominates the overtopping stage and the quasi-steady stage.

Nandasena et al. (2011b) reported three modes of initial transport of boulders or blocks under tsunami attack: sliding, rolling and saltation. When the flow velocity reaches the minimum velocity to initiate movement of the boulder, either of the transport modes above will occur (Nandasena et al., 2011b). In this study, an example of the tsunami flow-breakwater interaction was given in Fig. 5, the water splash-up entrained some Akmon units on the seaward side toe of the breakwater and deposited them on top of the breakwater (saltation). The water flow subsequently washed away the displaced Akmon units, along with some Akmon units at a higher elevation in the overtopping stage and the quasi-steady overflow stage (rolling and sliding). The major movement of Akmon units and the crown concrete units occurred before the maximum depth of the tsunami bore occurred, which could be explained by the larger velocities (Fig. 4b) or the specific momentum flux (Fig. 4d) in a tsunami bore at its leading front (Johnson et al., 2016; Nandasena et al., 2011a; Park et al., 2013; Xu et al., 2018). The units of the breakwater were not moved by the flow at the end of the quasi-steady overflow stage, even though in the quasi-steady stage the flow may have a larger water depth than the incoming supercritical flow. A preliminary experiment showed that a longer bore would not move more units in the breakwater.

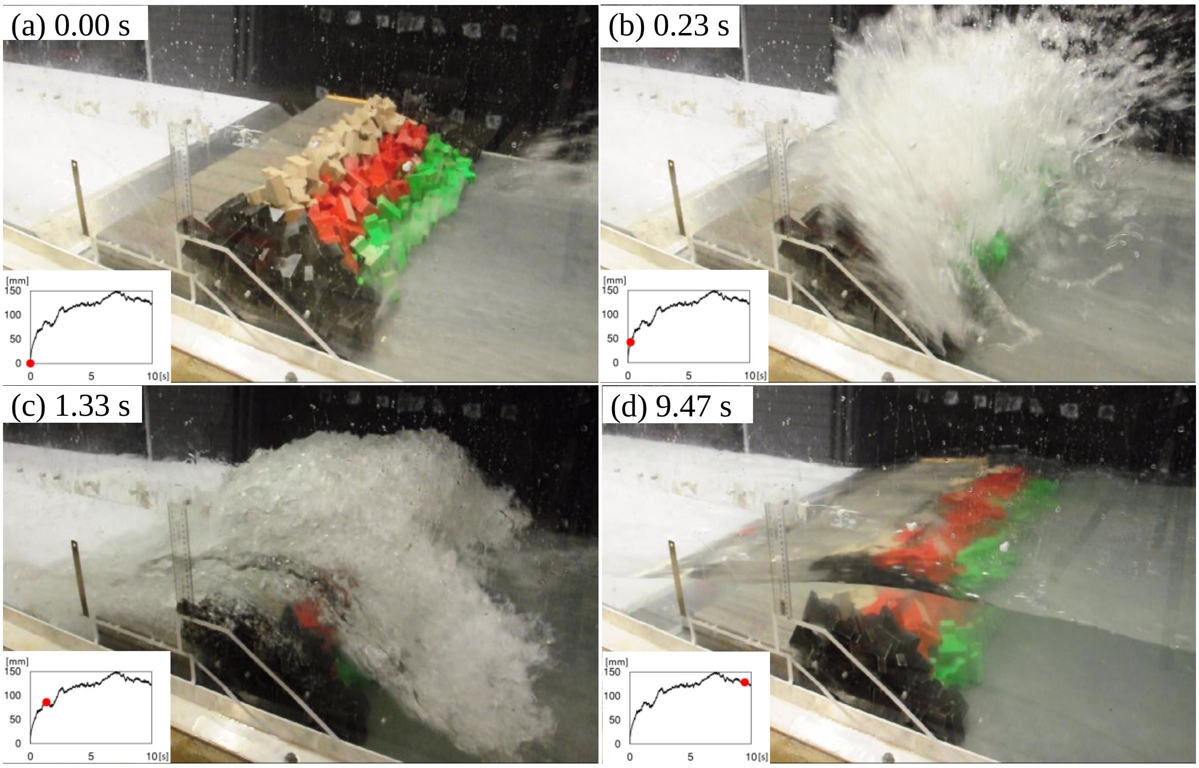

Fig. 5 Lateral view of the breakwater under dam-break simulated tsunamis. (a) Initial impact at 0.00 s. (b) Splash up at 0.23 s. (c) Overtopping at 1.33 s. (d) Quasi-steady overflow at 9.47 s. The height of the breakwater is 116 mm and the bore is case c (Table 3). The inset pictures show the bore depths at corresponding times without the breakwater.

3.3. General description of breakwater damage

For each of the bore depths tested, the damage to the breakwater can be classified into four failure stages: (1) initiation of movement of the concrete armour units; (2) displacement and washing away of the under layer (limestone rocks); (3) rotation and washing away of the crown concrete blocks; and (4) displacement of the precast concrete blocks. Stage 4 represents the collapse of the breakwater. The mode of damage of the breakwater was consistent for different breakwater heights and bore depths. There was some variability in the damage that occurred for different trials of the same scenario (Fig. 6). The values of damage parameter S and damage ratio R_d obtained for each scenario are therefore given as averages of five trials.

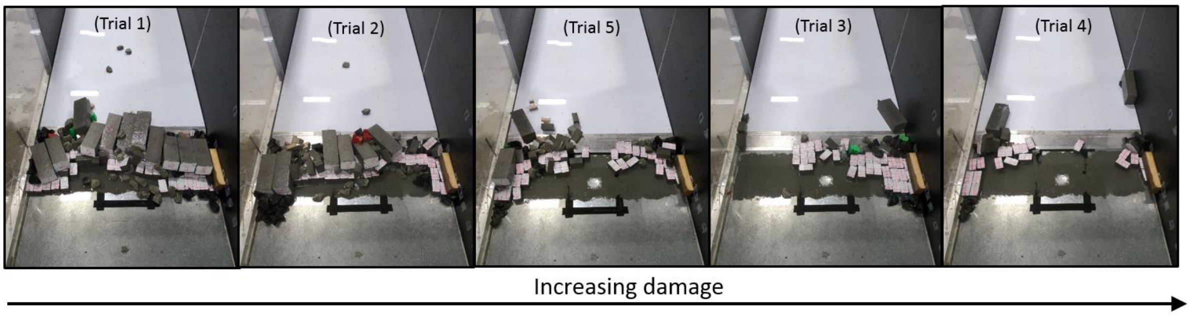

Fig. 6 An example of the variability of damage between different trials. The breakwater height is 116 mm and the bore case is (f) (Table 3). The breakwater was restored to its initial condition before each trial.

3.4. Breakwater stability for different breakwater heights

Fig. 7 to Fig. 10 provides a visual overview of the breakwater damage for each trial and breakwater height, in which the photo (0) shows the initial condition before each test. Each of the post-test photographs shows the particular test from a set of five with the median amount of damage, and therefore comparable with the damage parameter derived for the scenario.

All of the seaside armour was fully submerged during overtopping except in two cases, bore case (a) (Table 3) impacting the breakwater heights 202 mm and 245 mm. In these two scenarios, some Akmon units above the crest level of the crown blocks were not submerged, none of the armour units moved and no damage was observed. In all tests, around 40 yellow Akmon units were above the crest level of the crown blocks for each model, and were more easily moved by the overtopping flow. The crown concrete blocks remained stable until almost all seaside Akmon units and some limestone rocks were washed away. The precast concrete blocks under the crown blocks remained stable as long as the crown blocks were not displaced. For the breakwater damage caused by the 2011 Japan Tsunami, S=15 defined catastrophic damage (Esteban et al., 2014). This threshold is similar to the results in this study, in which almost all Akmon units were washed away when S>15 (except in the case with a breakwater height of 245 mm).

3.4.1 Breakwater height 116 mm

Only Akmon units were moved when the bore depth was less than 148 mm. Some limestone rocks were extracted when the bore depth was larger than 148 mm. When impacted by a 165 mm bore, almost all Akmon units and limestone rocks were washed away by the splashing flow (Fig. 7e). Immediately after that, the crown concrete blocks moved slightly backwards, the seaside edges of blocks lifted and each of the row of blocks rotated 180° along the long axis and were subsequently washed away. Once the precast concrete blocks underneath the crown blocks were exposed, they were easily displaced by the tsunami flow. Some precast concrete blocks were also extracted when the bore depth was 165 mm. The seaside row of the precast concrete blocks was more easily extracted once the other components of the protection structure were washed away.

3.4.2 Breakwater height 159 mm

Some limestone rocks were extracted when the bore depth was 156 mm (Fig. 8d), and. the crown blocks started to move when the bore depth was 200 mm (Fig. 8f). The precast concrete blocks started to be extracted when the bore depth was 220 mm (Fig. 8g). The top layer of precast concrete blocks was the first to be moved, and once it was washed away, the exposed seaside row of the bottom layer was also subject to movement.

3.4.3 Breakwater height 202 mm

Some limestone rocks were extracted when the bore depth was 165 mm (Fig. 9e). The crown blocks started to move when the bore depth was 200 mm (Fig. 9f). Some of the precast concrete blocks in the top layer, especially the seaward row, were extracted when the bore depth was 220 mm (Fig. 9g). No damage was observed in the middle layer and the bottom layer of the precast blocks.

3.4.4 Breakwater height 245 mm

The Akmon units started to move when the bore depth was 120 mm (Fig. 10b). Some limestone rocks were extracted when the bore depth was 200 mm (Fig. 10f). The crown blocks started to move when the bore depth was 220 mm (Fig. 10g), but no movement of precast concrete blocks was observed (even though almost all Akmon units were washed away).

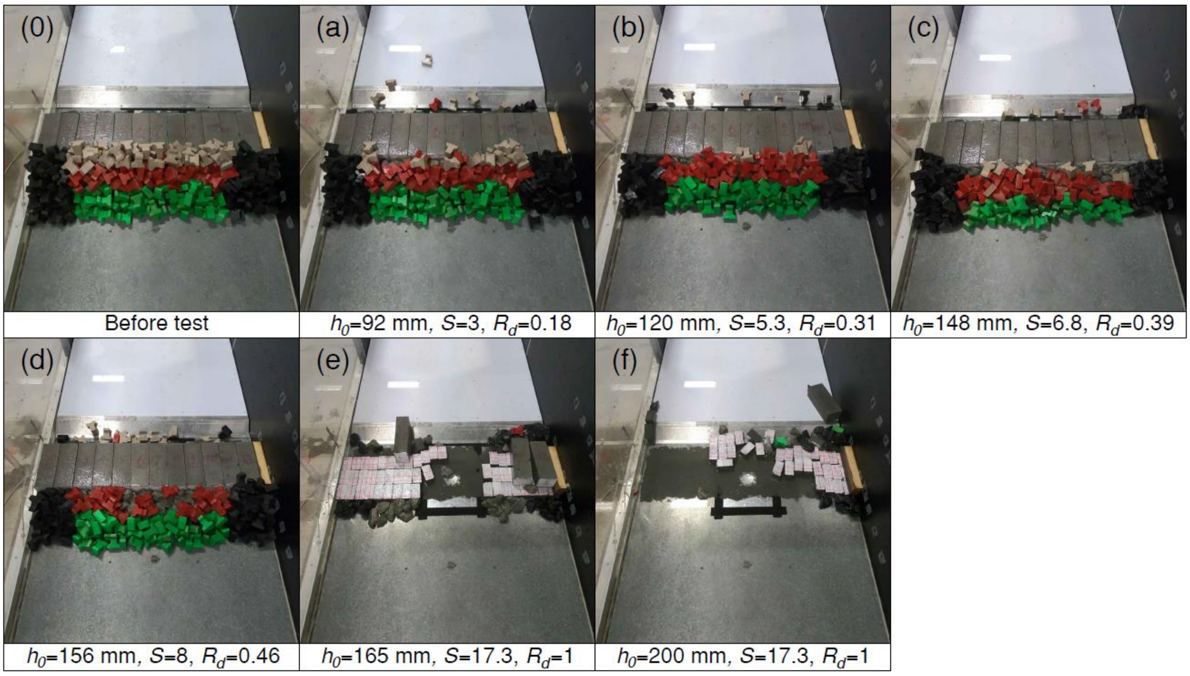

Fig. 7 Photos of damage of armour layer and breakwater units under different tsunami depths (a-f), breakwater height 116 mm.

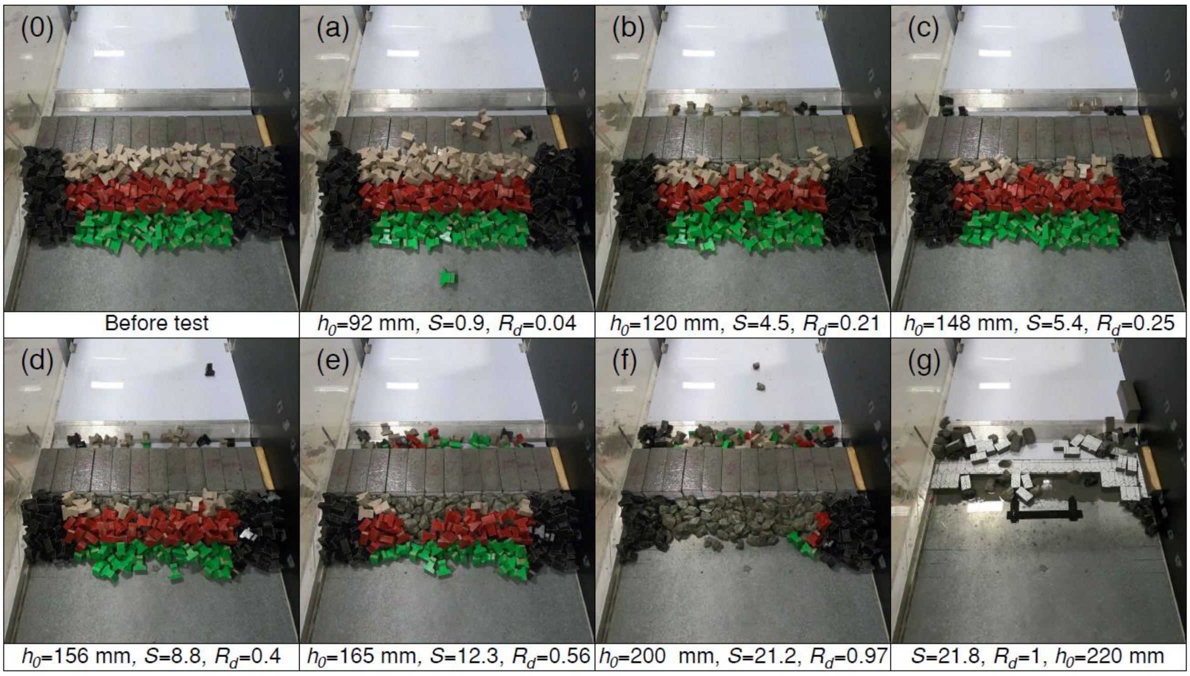

Fig. 8 Photos of damage of armour layer and breakwater units under different tsunami depths (a-g), breakwater height 159 mm.

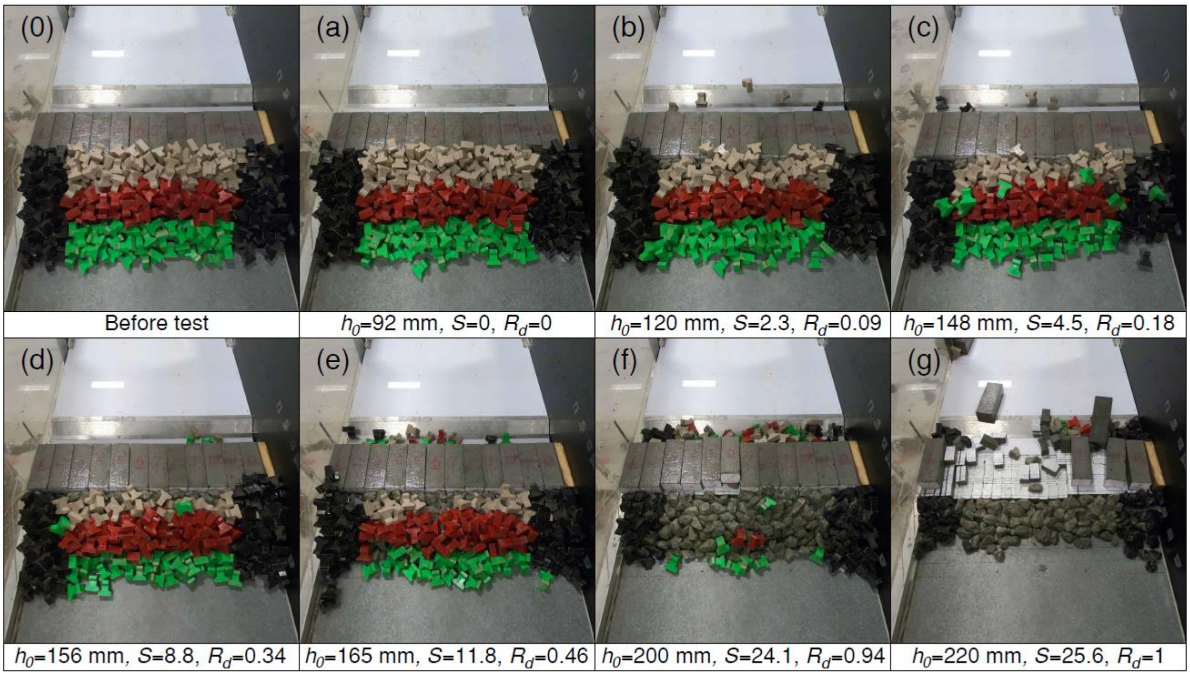

Fig. 9 Photos of damage of armour layer and breakwater units under different tsunami depths (a-g), breakwater height 202 mm.

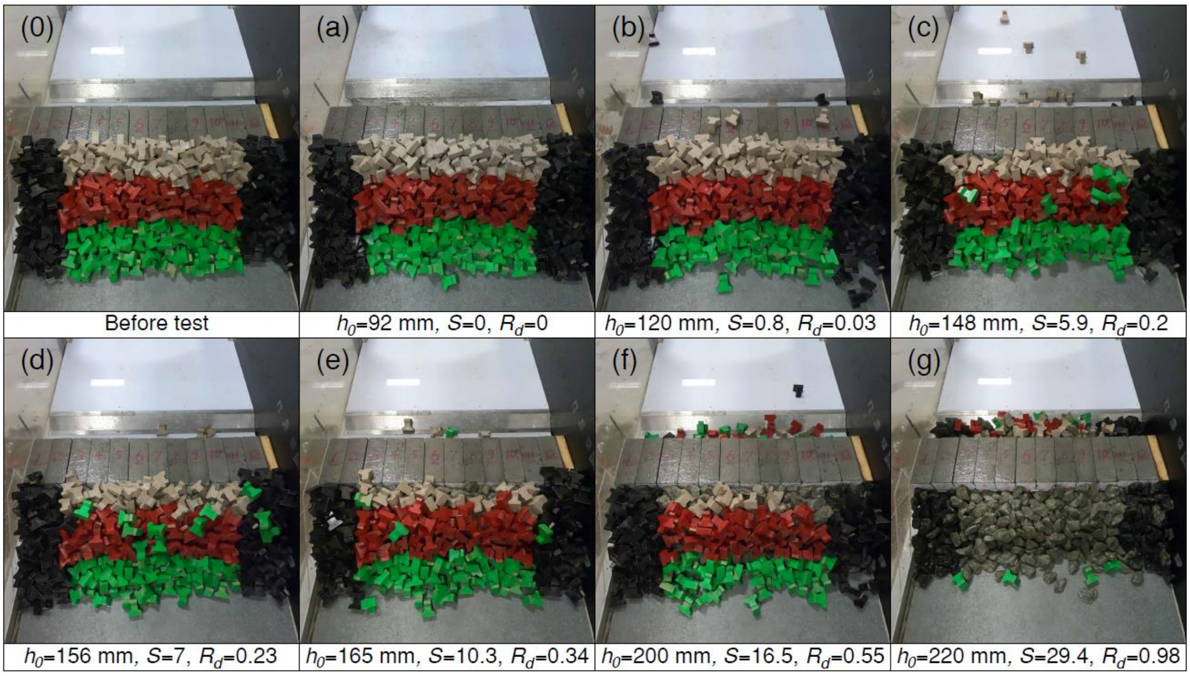

Fig. 10 Photos of damage of armour layer and breakwater units under different tsunami depths (a-g), breakwater height 245 mm.

3.5. Damage parameter, S

Analyses of the damage parameter *S* of the Akmon units are presented in this section. The largest *S* values obtained for breakwater heights 116 mm, 159 mm, 202 mm and 245 mm, were 17.3, 21.8, 25.6 and 30 respectively. The crown concrete blocks, which were protected by the armour layer, moved when *S* exceeded about 15 (except for the breakwater height of 245 mm). It is also apparent that total removal of the Akmon layer occurs at a larger value of *S* for a larger breakwater height, compared to that of a lower breakwater height. Fig. 11 shows the relationship between the damage parameter and (a) the bore depth h_0, and (b) the stability number, N_s. Typically, *S* increases with the bore depth and therefore with N_s. For the threshold for significant damage (S=15), N_s varies from 2.5 to 3.0 for breakwater height ranging from 116 mm to 245 mm. Fig. 12 (c) and (d) show the relationship of the damage parameter with the two non-dimensional parameters F_n and F_b, and show that the damage was smaller with a larger breakwater height and with a smaller bore strength. In general, the damage in terms of *S* decreases with increasing F_n or F_b. F_b is shown to be a better parameter to characterise damage compared to F_n, because *S* values are more scattered in the S-F_n graph. When F_b>1, little damage occurred. A surge in *S* occurs when F_b is decreased from 1. When F_b was as low as 0.5, destruction of the armour layer was observed. In summary, F_b is a useful parameter for assessing the damage of the armour layer under tsunami flow.

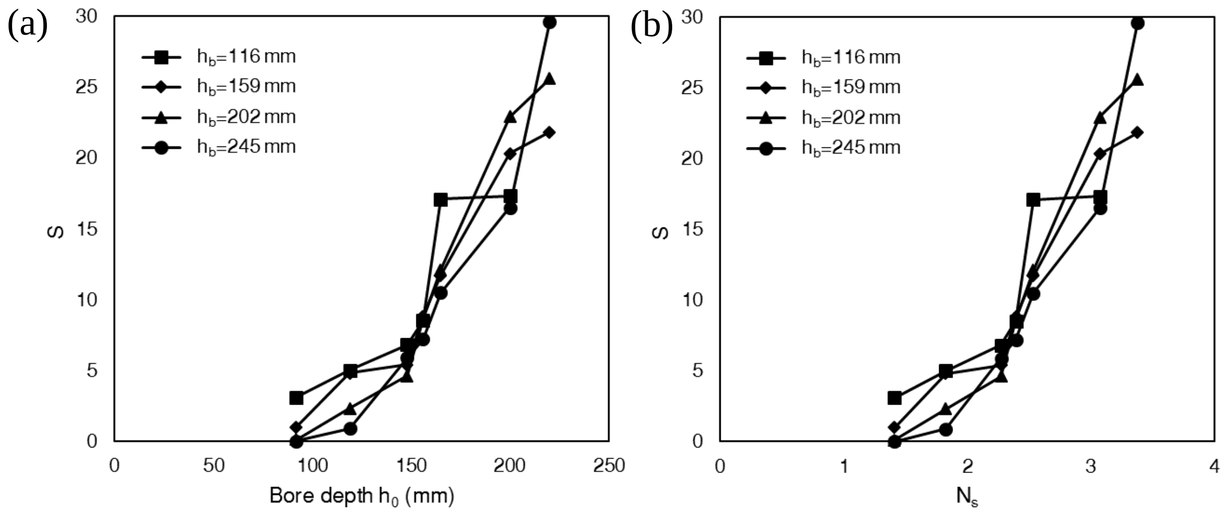

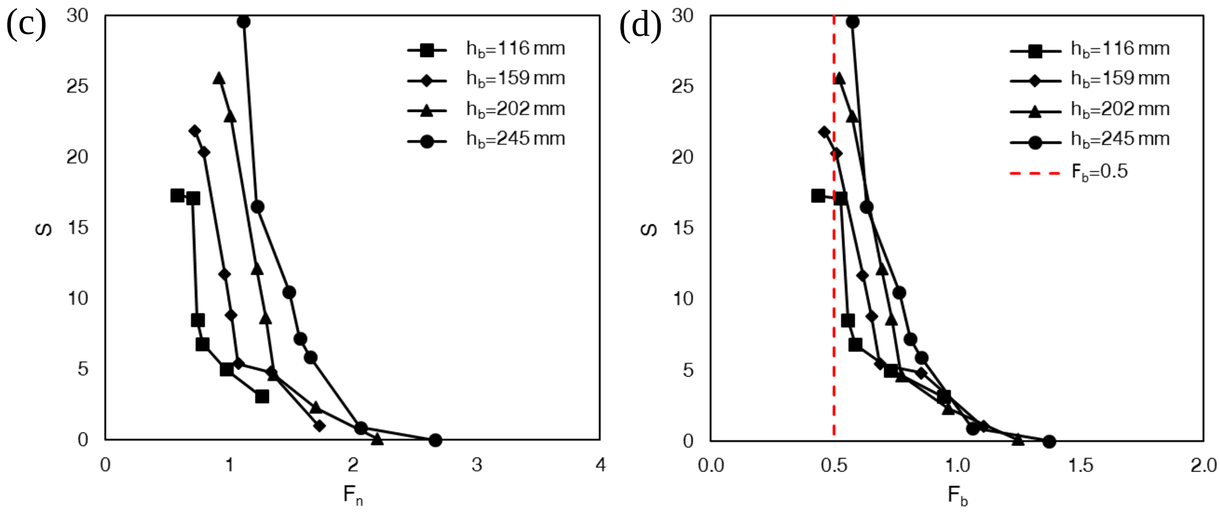

Fig. 11 Damage parameter S in relation to (a) h_0, (b) N_s , (c) F_n , (d) F_b

3.6. Damage ratio, R_d

The damage ratio R_d is plotted against the bore depth h_0, N_s, F_n and F_b in Fig. 12. R_d increases with the increasing bore depth and therefore increasing N_s. When N_s>2.3, R_d increases at a faster rate with N_s, reflecting increased damage with smaller increments in bore depth. Fig. 12 (c) and (d) show the relationship of the damage ratio with the two non-dimensional parameters F_n and F_b, again showing that the damage will be less with a larger breakwater height or a smaller bore strength. This again suggests that F_b is a good parameter for assessing the damage of the armour layer under tsunami flow as the data points are less scattered in the R_d-F_b graph than in the R_d-F_n graph. For the same N_s, the higher breakwaters experience less damage level; the higher breakwaters experience a delayed initiation of the same damage level, showing increased stability during the tsunami flow.

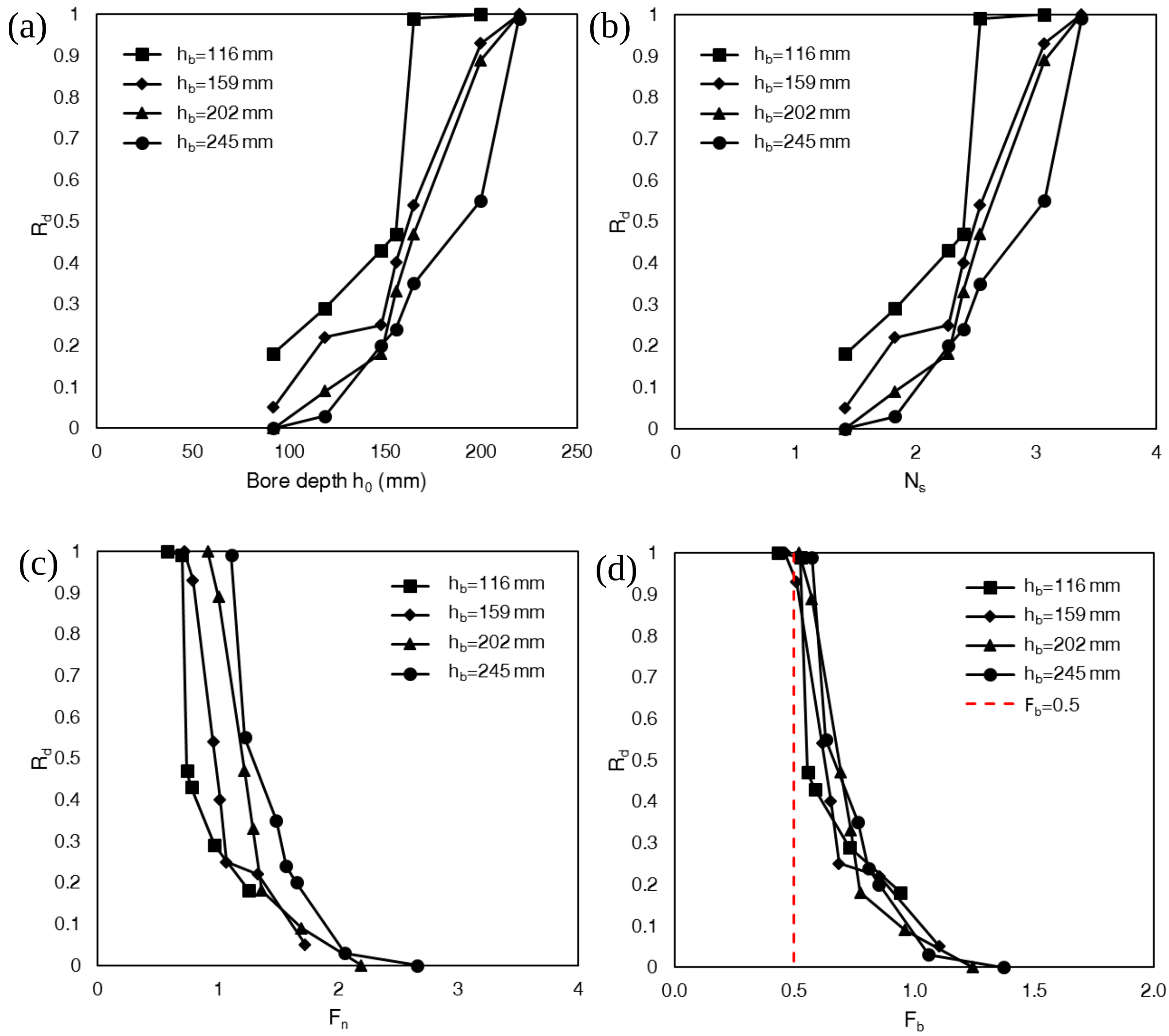

Fig. 12 Damage ratio R_d in relation to (a) h_0, (b) N_s , (c) F_n , (d) F_b

4. Discussion and implications

4.1. Froude number and the influence of bed roughness

Because no time-varying *Fr* records are available at the shoreline for actual tsunamis, many researchers reported *Fr* calculated from inundation flow depths and estimated inland velocities. For example, Nanayama and Shigeno (2006) estimated *Fr*=1.6-2.8 near a river mouth struck by the 1993 tsunami in southwest Hokkaido, Japan. When the flow travelled further inland, it became subcritical with *Fr*=0-0.9. Matsutomi et al. (2006) reported *Fr* from 0.7 to 2.0 in Thailand and Indonesia during the 2004 Indian Ocean Tsunami. Values of *Fr*=0.61~1.04 estimated from videos within Banda Aceh more than 3 km from the shoreline during the 2004 Indian Ocean Tsunami are reported by Fritz et al. (2006). Similarly, Nandasena et al. (2012) reported a Froude number of 1.14-1.4, estimated from videos, at a distance of 1 km inland from the shoreline at the Sendai plains. From numerical modelling of a tsunami approaching the coast under ideal conditions, *Fr* of the wave front increases at the shoreline due to a decreasing water depth and decreases as the flow propagates inland (Nandasena et al., 2013). With increased bed resistance and a sloping upward bed, the flow decelerates and steepens as the tsunami flow inundates inland areas (Esteban et al., 2019). As discussed above, a large *Fr* in the bore front that lasts for a short period (3-4 s) and *Fr*=1.05-1.6 in the quasi-steady state were deemed appropriate in this study (see Fig. 4c).

For the experiments, most parts of the surface of the channel were concrete with a Manning's roughness coefficient of 0.012. In the test section (2.4 m along the flow direction), the surface of the channel was smooth steel. Most recent experimental research by Wüthrich et al. (2019) and Esteban et al. (2019) showed that bores on a rough dry bed have lower front velocities, higher flow depths, lower *Fr* and steeper fronts. As the flow propagates inland, it seems necessary to increase the bed roughness to account for the macro-roughness such as urban buildings, vegetation etc., as suggested by Bricker et al. (2015).

4.2. Damage comparison

Aniel-Quiroga et al. (2018) proposed the equation below to estimate the damage in the seaside armour layer of rubble mound breakwaters under the impact of solitary waves,

$$\frac{S}{N} = 0.00678 F_n^{-1} \exp(1.191 N_s) \tag{10}$$

where S is the damage parameter, N is the number of waves, F_n is the freeboard (breakwater height herein) divided by wave height (bore depth herein) and N_s is the stability number. When N=1, the calculated S using this equation was much smaller than the measured S from the experiments of this study. This indicates dam-break simulated bores can cause more damage in the armour layer than solitary waves of the same height, which may attribute to higher velocities and longer durations of the bores, as well as the difference of the layout of the armour layer, slopes and types of units. In the wave overflow of the rubble mound breakwater, little damage was noticed on the seaside slope of the rubble mound breakwaters tested (Aniel-Quiroga et al., 2018), consistent with the little damage observed at the end of the quasi-steady overflow stage in this study.

4.3. Implications for design purposes and future research

The S-F_b and R_d-F_b graphs provide useful guidance to assess the potential damage to the armour layer of a similar composite breakwater given the tsunami depth, the breakwater height, the size and the density of armour units. In addition, if a minimum damage level under a certain tsunami depth is required, F_b should be greater than a certain value.

Many more factors may also affect the stability of composite breakwaters, e.g., seaward slopes, leeward erosion, types and sizes of armour units, which requires further research. To strengthen the stability of a similar composite breakwater tested in this study, many measures can be taken, e.g., clamping the crown concrete blocks, using larger armour units.

Esteban et al. (2014) pointed out the importance of including overtopping depths to predict failure of a breakwater. This is significant due to the lack of accurate measurements of the tsunami flow depth on land, as well as at the shoreline or in front of a breakwater. The maximum flow depth of tsunamis is usually estimated by water, mud or debris marks on structures and damage to structures (Nandasena et al., 2012). The transition of the supercritical incoming flow near the shoreline to a subcritical flow when the flow propagates further inland or when confronting a barrier would be accompanied by an increase in the water depth, as this study implies. Future research can be conducted to relate the maximum flow depth to the damage of the breakwater.

5. Conclusions

A scale model of a composite breakwater in New Zealand was reproduced in the dam-break tsunami channel at the University of Auckland. A range of bore depths and breakwater heights were investigated to understand the tsunami bore-breakwater interaction and determine the stability of the breakwater.

Four stages were observed when the tsunami bore impacted the breakwater: initial impact, splash up, overtopping and quasi-steady overflow. Damage to the breakwater was initiated by movement of the concrete armour units, then displacement and washing away of the under layer (limestone rocks), washing away of the crown concrete blocks, and subsequent displacement of the precast concrete blocks. The damage parameter S and the damage ratio R_d increase with bore depths and N_s. The higher breakwaters experience delayed initiation of the same damage levels (S and R_d). Plotting S and R_d against the newly proposed parameter F_b is a good method for assessing the damage of the armour layer under tsunami flow. Little damage of armour layer was observed when $F_b>1$ while destruction occurred when F_b approached 0.5.

Data Availability Statement

All data, models, and code generated or used during the study appear in the submitted article.

Acknowledgements

This work was funded by Natural Hazards Research Platform and Napier Port Ltd. The authors would like to thank Dan Fray and Geoff Kirby for their help in the experimental setup and Graham Macky for his advice to improve the manuscript. The authors thank the two anonymous reviewers for their help in revising the manuscript.

Notation

The following symbols are used in this paper:

a, b, c = lengths of longitudinal, lateral, and height axes of concrete blocks (m);

A = surface area of the armour layer (m^2);

A_e = average eroded area (m^2);

d = thickness of the armour layer (m);

D_{n50} = cube-equivalent side length of the unit (m);

F_b = ratio of the stabilising strength of the armour units to the bore depth;

F_n = ratio of the breakwater height over the bore depth (relative breakwater height);

Fr = Froude number;

g = acceleration of gravity (m/s^2);

GO = gate opening height (m);

H = reservoir water depth (m);

h_b = breakwater height (m);

h_0 = maximum bore depth (m);

L = width of the studied section (m);

m = number of armour units;

n = armour layer bulk porosity;

N = number of waves;

$N_{displaced}$ = number of displaced stones/units;

N_{total} = total number of stones/units;

N_e = number of extracted stones;

N_s = stability number;

R_d = damage ratio;

RWL = reservoir water level (m);

S = damage parameter;

T = tsunami wave period (s);

u = flow velocity (m/s);

U = bore tip velocity (m/s);

V = volume of a single armour unit (m^3)

W_{50} = median stone weight (kg);

λ_W = weight scale;

λ_L = length scale;

λ_T = time scale;

$(\gamma_r)_m$ = unit weight of stones in model (kg/m^3);

$(\gamma_r)_p$ = unit weight of stones in prototype (kg/m^3);

$(\gamma_W)_m$ = unit weight of water in model (kg/m^3);

$(\gamma_W)_p$ = unit weight of water in prototype (kg/m^3);

ρ_s = density of the breakwater units (kg/m^3);

ρ_w = density of water (kg/m^3);

Δ = relative mass density.

Reference

Aniel-Quiroga, Í., Vidal, C., Lara, J.L., González, M., Sainz, Á., 2018. Stability of rubble-mound breakwaters under tsunami first impact and overflow based on laboratory experiments. Coast. Eng. 135, 39–54. doi:10.1016/j.coastaleng.2018.01.004

Arikawa, T., Sato, M., Shimosako, K., Hasegawa, I., Yeom, G.-S., Tomita, T., 2012. Failure Mechanism of Kamaishi Breakwaters due to the Great East Japan Earthquake Tsunami. Coast. Eng. Proc. 1, 13. doi:10.9753/icce.v33.structures.16

Bricker, J.D., Gibson, S., Takagi, H., Imamura, F., 2015. On the Need for Larger Manning ' s Roughness Coefficients in Depth-Integrated Tsunami Inundation Models. Coast. Eng. J. 57, 1550005. doi:10.1142/S0578563415500059

Broderick, L., 1984. Riprap stability versus monochromatic and irregular waves. George Washington University. doi:10.1300/J082v36n01

Chanson, H., 2006. Tsunami Surges on Dry Coastal Plains: Application of Dam Break Wave Equations. Coast. Eng. J. 48, 355–370. doi:10.1142/S0578563406001477

Chen, C., Melville, B.W., Nandasena, N.A.K., 2018. Investigations of Reduction Effect of Vertical Wall on Dam-Break-Simulated Tsunami Surge Exerted on Wharf Piles. J. Earthq. Tsunami 12, 1840006. doi:10.1142/S1793431118400067

Chen, C., Melville, B.W., Nandasena, N.A.K., Shamseldin, A.Y., Wotherspoon, L., 2016. Experimental study of uplift loads due to tsunami bore impact on a wharf model. Coast. Eng. 117, 126–137. doi:10.1016/j.coastaleng.2016.08.001

Downes GL, Webb T, McSaveney M et al. (2000). The 26 March and 17 May 1947 Gisborne earthquakes and tsunami: implications for tsunami hazard for the east coast, North Island, New Zealand. In: Proceedings of the international tsunami workshop tsunami risk assessment beyond 2000: Theory, Practice and Plans, pp 55–67

Eiby, G.A., 1982. Two New Zealand tsunamis. J. R. Soc. New Zeal. 12, 337–351. doi:10.1080/03036758.1982.10415340

Esteban, M., Glasbergen, T., Takabatake, T., Hofland, B., Nishizaki, S., Nishida, Y., Stolle, J., Nistor, I., Bricker, J., Takagi, H., Shibayama, T., 2017. Overtopping of Coastal Structures by Tsunami Waves. Geosciences 7, 121. doi:10.3390/geosciences7040121

Esteban, M., Jayaratne, R., Mikami, T., Morikubo, I., Shibayama, T., Thao, N.D., Ohira, K., Ohtani, A., Mizuno, Y., Kinoshita, M., Matsuba, S., 2014. Stability of breakwater armor units against tsunami attacks. J. Waterw. Port, Coastal, Ocean Eng. 140, 188–198. doi:10.1061/(asce)ww.1943-5460.0000227

Esteban, M., Roubos, J.J., Iimura, K., Salet, J.T., Hofland, B., Bricker, J., Ishii, H., Hamano, G., Takabatake, T., Shibayama, T., 2019. Effect of bed roughness on tsunami bore propagation and overtopping. Coast. Eng. 103539. doi:10.1016/j.coastaleng.2019.103539

Fraser, R.J., 1998. Historical Tsunami Database for New Zealand. University of Waikato.

Fraser, S. a., Power, W.L., Wang, X., Wallace, L.M., Mueller, C., Johnston, D.M., 2014. Tsunami inundation in Napier, New Zealand, due to local earthquake sources. Nat. Hazards 70, 415–445. doi:10.1007/s11069-013-0820-x

Fritz, H.M., Borrero, J.C., Synolakis, C.E., Yoo, J., 2006. 2004 Indian Ocean tsunami flow velocity measurements from survivor videos. Geophys. Res. Lett. 33, 3–7. doi:10.1029/2006GL026784

Fritz, H.M., Kongko, W., Moore, A., McAdoo, B., Goff, J., Harbitz, C., Uslu, B., Kalligeris, N., Suteja, D., Kalsum, K., Titov, V., Gusman, A., Latief, H., Santoso, E., Sujoko, S., Djulkarnaen, D., Sunendar, H., Synolakis, C., 2007. Extreme runup from the 17 July 2006 Java tsunami. Geophys.

Res. Lett. 34, 1–5. doi:10.1029/2007GL029404

Fritz, H.M., Petroff, C.M., Catal?n, P.A., Cienfuegos, R., Winckler, P., Kalligeris, N., Weiss, R., Barrientos, S.E., Meneses, G., Valderas-Bermejo, C., Ebeling, C., Papadopoulos, A., Contreras, M., Almar, R., Dominguez, J.C., Synolakis, C.E., 2011. Field Survey of the 27 February 2010 Chile Tsunami. Pure Appl. Geophys. 168, 1989–2010. doi:10.1007/s00024-011-0283-5

GNS Science, 2013. Review of Tsunami Hazard in New Zealand (2013 Update), GNS Science Report.

Gómez-Martín, M.E., Medina, J.R., 2013. Heterogeneous Packing and Hydraulic Stability of Cube and Cubipod Armor Units. J. Waterw. Port, Coastal, Ocean Eng. 140, 100–108. doi:10.1061/(asce)ww.1943-5460.0000223

Goto, K., Chavanich, S.A., Imamura, F., Kunthasap, P., Matsui, T., Minoura, K., Sugawara, D., Yanagisawa, H., 2007. Distribution, origin and transport process of boulders deposited by the 2004 Indian Ocean tsunami at Pakarang Cape, Thailand. Sediment. Geol. 202, 821–837. doi:10.1016/j.sedgeo.2007.09.004

Guler, H.G., Arikawa, T., Oei, T., Yalciner, A.C., 2015. Performance of rubble mound breakwaters under tsunami attack, a case study: Haydarpasa Port, Istanbul, Turkey. Coast. Eng. 104, 43–53. doi:10.1016/j.coastaleng.2015.07.007

Isbash, S. V. (1936). Construction of dams by depositing rock in running water. Second congress on large dams, Washington, DC, 123–136.

Jayaratne, M.P.R., Premaratne, B., Adewale, A., Mikami, T., Matsuba, S., Shibayama, T., Esteban, M., Nistor, I., 2016. Failure Mechanisms and Local Scour at Coastal Structures Induced by Tsunami. Coast. Eng. J. 58, 1640017. doi:10.1142/S0578563416400179

Johnson, J.P.L., Delbecq, K., Kim, W., Mohrig, D., 2016. Experimental tsunami deposits: Linking hydrodynamics to sediment entrainment, advection lengths and downstream fining. Geomorphology 253, 478–490. doi:10.1016/j.geomorph.2015.11.004

Kato, F., Suwa, Y., Watanabe, K., Hatogai, S., 2012. Mechanisms of coastal dike failure induced by the Great East Japan Earthquake Tsunami. Coast. Eng. Proc. 1, 1–9. doi:10.9753/icce.v33.structures.40

King, D.N., 2015. Tsunami hazard, assessment and risk in Aotearoa-New Zealand: A systematic review AD 1868-2012. Earth-Science Rev. 145, 25–42. doi:10.1016/j.earscirev.2015.02.004

Klettner, C., Balasubramanian, S., Hunt, J., Fernando, H., Voropayev, S., Eames, I., 2012. Draw-down and run-up of tsunami waves on sloping beaches, in: Proceedings of the ICE - Engineering and Computational Mechanics. pp. 119–129. doi:10.1680/eacm.10.00044

Lekkas, E., Andreadakis, E., Alexoudi, V., Kapourani, E., Kostaki, I., 2011. The Mw=9.0 Tohoku Japan Earthquake (March 11, 2011) Tsunami Impact on Structures and Infrastructure. Environ. Geosci. Eng. Surv. Territ. Prot. Popul. Saf. Int. Conf. 97–103.

Losada, M.A., Desire, J.M., Alejo, L.M., 1986. Stability of blocks as breakwater armor units. J. Struct. Eng. 112, 2392–2401. doi:10.1061/(asce)0733-9445(1986)112:11(2392)

Maruyama, S., Mitsui, J., Matsumoto, A., Hanzawa, M., 2014. Armor damage on harbor side rubble mound of composite breakwaters against water jet caused by impinging bore-like tsunami, in: Coastal Engineering Proceedings. pp. 2–7.

Matsutomi, H., Sakakiyama, T., Nugroho, S., Matsuyama, M., 2006. Aspects of inundated flow due to the 2004 indian ocean tsunami. Coast. Eng. J. 48, 167–195.

Mitsui, J., Matsumoto, A., Hanzawa, M., Nadaoka, K., 2016. Estimation Method of Armor Stability Against Tsunami Overtopping Caisson Breakwater Based on Overflow Depth. Coast. Eng. J. 58. doi:10.1142/S0578563416400192

Mitsui, J., Matsumoto, A., Hanzawa, M., Nadaoka, K., 2014. Stability of armor units covering rubble mound of composite breakwaters against a steady overflow of tsunami. Coast. Eng. Proc. 1, 34. doi:10.9753/icce.v34.structures.34

Nanayama, F., Shigeno, K., 2006. Inflow and outflow facies from the 1993 tsunami in southwest Hokkaido. Sediment. Geol. 187, 139–158. doi:10.1016/j.sedgeo.2005.12.024

Nandasena, N.A.K., Paris, R., Tanaka, N., 2011a. Numerical assessment of boulder transport by the 2004 Indian ocean tsunami in Lhok Nga, West Banda Aceh (Sumatra, Indonesia). Comput. Geosci. doi:10.1016/j.cageo.2011.02.001

Nandasena, N.A.K., Paris, R., Tanaka, N., 2011b. Reassessment of hydrodynamic equations: Minimum flow velocity to initiate boulder transport by high energy events (storms, tsunamis). Mar. Geol. 281, 70–84. doi:10.1016/j.margeo.2011.02.005

Nandasena, N.A.K., Sasaki, Y., Tanaka, N., 2012. Modeling field observations of the 2011 Great East Japan tsunami: Efficacy of artificial and natural structures on tsunami mitigation. Coast. Eng. doi:10.1016/j.coastaleng.2012.03.009

Nandasena, N.A.K., Tanaka, N., Sasaki, Y., Osada, M., 2013. Boulder transport by the 2011 Great East Japan tsunami: Comprehensive field observations and whither model predictions? Mar. Geol. 346, 292–309. doi:10.1016/j.margeo.2013.09.015

Ohtsu, I., Yasuda, Y., Hashiba, H., 1996. Incipient jump conditions for flows over a vertical sill. J. Hydraul. Eng. 122, 465–469.

Opus. Napier Port breakwater insurance valuation. 2018.

Ozmen-Cagatay, H., Kocaman, S., 2011. Dam-break flow in the presence of obstacle: Experiment and CFD simulation. Eng. Appl. Comput. Fluid Mech. 5, 541–552. doi:10.1080/19942060.2011.11015393

PARI, 2011. Urgent Survey for 2011 Great East Japan Earthquake and Tsunami Disaster in Ports and Coasts.

Paris, R., Fournier, J., Poizot, E., Etienne, S., Morin, J., Lavigne, F., Wassmer, P., 2010. Boulder and fine sediment transport and deposition by the 2004 tsunami in Lhok Nga (western Banda Aceh, Sumatra, Indonesia): A coupled offshore-onshore model. Mar. Geol. 268, 43–54. doi:10.1016/j.margeo.2009.10.011

Park, H., Cox, D.T., Lynett, P.J., Wiebe, D.M., Shin, S., 2013. Tsunami inundation modeling in constructed environments: A physical and numerical comparison of free-surface elevation, velocity, and momentum flux. Coast. Eng. 79, 9–21. doi:10.1016/j.coastaleng.2013.04.002

Port of Napier Limited, 2018. Napier port annual report 2018. Napier, New Zealand.

Robert Hudson, 1959. Laboratory investigation of rubbel-mound breakwaters, in: Journal of the Waterway and Harbors Division. p. 84. doi:10.1126/science.1.3.84

Shafiei, S., Melville, B.W., Shamseldin, A.Y., 2016. Experimental investigation of tsunami bore impact force and pressure on a square prism. Coast. Eng. 110, 1–16. doi:10.1016/j.coastaleng.2015.12.006

Tadepalli, S., Synolakis, C., 1996. Model for the Leading Waves of Tsunamis. Phys. Rev. Lett. 77, 2141–2144. doi:10.1103/PhysRevLett.77.2141

Takagi, H., Bricker, J.D., 2014. Assessment of the effectiveness of general breakwaters in reducing tsunami inundation in Ishinomaki. Coast. Eng. J. 56, 1–21. doi:10.1142/S0578563414500181

Takagi, H., Esteban, M., 2013. Practical methods of estimating tilting failure of caisson breakwaters using a Monte-Carlo simulation. Coast. Eng. J. 55, 1350011-1-1350011–22.

doi:10.1142/S0578563413500113

Van der Meer, J.W., 1987. Stability of breakwater armour layers - design formulae. Coast. Eng. 11, 219–239. doi:10.1016/0378-3839(87)90013-5

Vidal, B.C., Losada, M.A., Medina, R., 1991. Stability o f mound breakwater's head and trunk. J. Waterw. Port, Coastal, Ocean Eng. 117, 570–587.

Vidal, C., Martin, F.L., Negro, V., Gironella, X., Madrigal, B., Garcia-Palacios, J., 2004. Measurement of armour damage on rubble mound structures: comparison between different methodologies, in: Coastal Structures 2003. Americal Society of Civil Engineers, Reston, VA, pp. 189–200.

Vidal, C., Losada, M.A., Medina, R., Losada, E.I., 1994. Analisis de la estabilidad de diques rompeolas, vol. 1, pp. 17–34.

Wüthrich, D., Pfister, M., Schleiss, A.J., 2019. Effect of bed roughness on tsunami-like waves and induced loads on buildings. Coast. Eng. 152. doi:10.1016/j.coastaleng.2019.103508

Xu, Z., Nandasena, N.A.K., Whittaker, C.N., Melville, B.W., 2018. Numerical modelling of flow in Little Pigeon Bay due to the 2016 Kaikoura tsunami. Ocean Eng. 159, 228–236. doi:10.1016/j.oceaneng.2018.04.004